Nano Research
2022, 15(2): 1221–1229
ISSN 1998-0124 CN 11-5974/O4
https://doi.org/10.1007/s12274-021-3629-z

Research Article

# Modulating reaction pathways of formic acid oxidation for optimized electrocatalytic performance of PtAu/CoNC

Mengchao Liang[1,§], Tianyu Xia[1,§] (✉), Han Gao[1], Kai Zhao[1], Tianqi Cao[1], Meng Deng[1], Xiaoyan Ren[1], Shunfang Li[1], Haizhong Guo[1,2] (✉), and Rongming Wang[3] (✉)

[1] *Key Laboratory of Material Physics, Ministry of Education, School of Physics and Microelectronics, Zhengzhou University, Zhengzhou 450052, China*
[2] *Collaborative Innovation Center of Light Manipulations and Applications, Shandong Normal University, Jinan, Shandong 250358, China*
[3] *Beijing Advanced Innovation Center for Materials Genome Engineering, Beijing Key Laboratory for Magneto-Photoelectrical Composite and Interface Science, School of Mathematics and Physics, University of Science and Technology Beijing, Beijing 100083, China*
[§] *Mengchao Liang and Tianyu Xia contributed equally to this work.*


**Received:** 23 February 2021 / **Revised:** 18 May 2021 / **Accepted:** 30 May 2021

## ABSTRACT

Formic acid oxidation (FAO) is a typical anode reaction in fuel cells that can be facilitated by modulating its direct and indirect reaction pathways. Herein, PtAu bimetallic nanoparticles loaded onto Co and N co-doping carbon nanoframes (CoNC NFs) were designed to improve the selectivity of the direct reaction pathway for efficient FAO. Based on these subtle nanomaterials, the influences of elemental composition and carbon-support materials on the two pathways of FAO were investigated in detail. The results of fuel cell tests verified that the appropriate amount of Au in PtAu/CoNC can promote a direct reaction pathway for FAO, which is crucial for enhancing the oxidation efficiency of formic acid. In particular, the obtained PtAu/CoNC with an optimal Pt/Au atomic ratio of 1:1 (PtAu/CoNC-3) manifests the best catalytic performance among the analogous obtained Pt-based electrocatalysts. The FAO mass activity of the PtAu/CoNC-3 sample reached 0.88 $A \cdot mg_{Pt}^{-1}$, which is 26.0 times higher than that of Pt/C. The results of first-principles calculation and CO stripping jointly demonstrate that the CO adsorption of PtAu/CoNC is considerably lower than that of Pt/CoNC and PtAu/C, which indicates that the synergistic effect of Pt, Au, and CoNC NFs is critical for the resistance of Pt to CO poisoning. This work is of great significance for a deeper understanding of the oxidation mechanism of formic acid and provides a feasible and promising strategy for enhancing the catalytic performance of the catalyst by improving the direct reaction pathway for FAO.

## KEYWORDS

formic acid oxidation, direct oxidation pathway, metal organic framework, co-doping, CO binding energy

## 1 Introduction

With the depletion of fossil energy and increasing severity of environmental pollution, the development of sustainable energy conversion technologies such as fuel cells has attracted abundant research attention [1]. Among various fuel cells, direct formic acid fuel cells (DFAFCs) have been recognized as promising future energy devices with low toxicity, high energy density, and low crossover flux of fuels through the Nafion membrane [2, 3]. Thus far, Pt catalysts have played an irreplaceable role in catalyzing the formic acid oxidation (FAO) reaction, which determines the efficiency and stability of DFAFCs [4–6]. However, the scarce reserves and high prices of Pt largely limit its widespread applications in industrial production. Therefore, improving the utilization of Pt and enhancing its catalytic efficiency toward FAO are essential.

Adequate understanding of the mechanism of Pt-catalyzed FAO, which modulates the reaction pathway to obtain high current density, can effectively enhance the catalytic efficiency of Pt. Generally, the reaction of this FAO follows a dual-path mechanism of direct and indirect pathways. The direct pathway is the direct oxidation of formic acid to generate $CO_2$, whereas the indirect pathway includes the oxidation of formic acid to intermediate CO ($CO_{ads}$) and the subsequent oxidation of $CO_{ads}$ to final $CO_2$ at high potential. These pathways are referred to as dehydrogenation and dehydration reactions, respectively [7]. In a typical catalysis process, $CO_{ads}$ derived from formic acid dehydration can strongly adhere to and poison the electrode surface, thus reducing the amount of free Pt available for the direct pathway. In this case, the direct pathway is inhibited, and the catalyst activity is significantly reduced [8]. For this reason, there is an urgent need to limit the indirect oxidation pathway of formic acid, reduce the adsorption of $CO_{ads}$, and substantially facilitate the catalytic efficiency of the Pt catalyst.

In addition, the incorporation of other elements compounded with Pt beneficial for improving the catalytic efficiency of the Pt. This is because the introduction of other elements can reduce the dose of Pt and enhance its electrocatalytic performance by utilizing the geometric and electronic effects [9–12]. Among

Address correspondence to Tianyu Xia, tyxia@zzu.edu.cn; Haizhong Guo, hguo@zzu.edu.cn; Rongming Wang, rmwang@ustb.edu.cn

the series of Pt-based electrocatalysts, PtAu is particularly prominent because Au can improve the energy band structure of Pt and has a good synergistic effect with this element [13]. Moreover, the presence of Au can enhance the stability of Pt and prevent its easy dissolution in the catalytic reaction [11]. In recent years, extensive efforts have been devoted to enhance the electrocatalytic performance of PtAu catalysts by controlling their particle sizes, morphologies, and compositions [14–18]. For example, nanoporous PtAu alloys with low Pt content have been synthesized based on the dealloying strategy, and the mass activity of as-prepared PtAu is up to 113 times that of Pt/C [19]. Similarly, a surfactant-free and ultrasound-assisted method was used to prepare a PtAu/C system that exhibits excellent FAO activity of 14.5 $A{\cdot}mg_{Pt}^{-1}$ [20]. However, the mechanism inherent in the PtAu-catalyzed FAO reaction remains under debate; thus, further research and discussion are needed to provide a better understanding of this mechanism.

Moreover, the loading of metal nanoparticles (NPs) on suitable support materials has proved to be a feasible option for enhancing the FAO performance of Pt-based catalysts [20, 21]. Several common carbon materials such as carbon nanotubes, carbon nanofibers, graphene, and metal organic framework (MOF) derivatives are considered to be ideal support materials owing to their high specific surface area, high stability, and strong electrical conductivity [15, 22]. Recently, heteroatom-doped MOF derivatives have attracted abundant attention in the electrocatalytic field, particularly co-doping that consists of both transition metal and nonmetallic elements. Such products facilitate the formation of metal-(nonmetallic)$_x$ active sites and thus improve the catalytic activity of the catalyst [23]. For example, the $Pt_2Co_8$@N–C nanorod array catalyst prepared by Ren et al. through carbonization of the precursor ZIF-67 has shown good electrocatalytic activity and long-term stability for electrochemical reactions [24]. However, little research is available on the application of heteroatom co-doped MOF derivatives as catalytic support material for FAO reactions in acidic solutions.

Inspired by this, we herein successfully design and synthesize a series of supported PtAu catalysts with designated Pt/Au ratios including PtAu loaded onto Co and N co-doped MOF-derived carbon-containing nanoframes (CoNC NFs). The morphology, structure, and catalytic performance of the PtAu/CoNC are characterized and discussed in detail. More importantly, the PtAu/CoNC samples are used as a model system to reveal the effect of different Au contents on the two oxidation pathways of FAO. We determine that a Pt/Au ratio of 1:1 with the support of CoNC NFs enables the optimal FAO catalytic performance to be obtained compared with the performances of as-prepared PtAu/C and PtAuCo/C.

## 2 Experimental

### 2.1 Preparation of ZIF-67

In this study, 5 mmol of cobalt nitrate hexahydrate ($Co(NO_3)_2{\cdot}6H_2O$) and 40 mmol of 2-methylimidazole ($C_4H_6N_2$) were dissolved in 100 mL of anhydrous methanol; these solutions were labeled as A and B, respectively. After stirring for 10 min, solution A was quickly poured into solution B. The color of the solution changed from blue to dark purple, and then the reaction continued at room temperature (RT) for 24 h. After the reaction was completed, the purple precipitate was collected by centrifugation, washed with anhydrous methanol, and dried under a vacuum at 70 °C overnight to obtain the purple ZIF-67 powder.

### 2.2 Preparation of CoNC NFs

To prepare the CoNC NFs, 200 mg of ZIF-67 was placed in a plasma-enhanced chemical vapor deposition, and the tube was evacuated with Ar gas. After heating from RT to 350 °C and maintaining the temperature for 1 h, the temperature was further raised to the next target temperature of 600 °C at a heating rate of 2 $°C{\cdot}min^{-1}$. After the temperature was held for 2 h, the furnace was naturally cooled to RT, and the black powder product was treated in a 0.5 M $H_2SO_4$ solution for 6 h. The obtained CoNC NFs samples were collected by centrifugation, washed with deionized water, and then dried at 70 °C.

### 2.3 Synthesis of PtAu/CoNC, PtAu/C, and PtAuCo/C

For the product synthesis, $x$ mL of aqueous $K_2PtCl_6$ (5 mM), 1 mL of aqueous ascorbic acid (100 mM), and 3 mg of CoNC NFs powder were added to 30 mL of ethanol. Then, $y$ mL of aqueous $NaBH_4$ (25 mM) was added drop by drop, and the mixed solution was subjected to continuous mechanical stirring and an ultrasonic bath to ensure a smooth reaction. After 15 min, $z$ mL of aqueous $HAuCl_4{\cdot}4H_2O$ (5 mM) was also added drop by drop. After 15 min of thorough reaction, the black products were washed with ethanol and were dried in a vacuum oven at 70 °C for 24 h. For Pt/CoNC and PtAu/ CoNC-1, -2, and -3, the values of $x$–$y$–$z$ were 1–1–0, 1–1–0.25, 1–1–0.5, and 1–1–1, respectively. The same method was used to synthesize the series of PtAu/C samples by replacing the CoNC NFs with Vulcan XC 72R carbon black. For the PtAuCo/C, the value of $x$–$y$–$z$ was 1–1–1, and the Co precursors ($CoCl_2{\cdot}6H_2O$, 5 mM) were added together with Pt precursors.

### 2.4 Materials characterization

The morphologies and crystal structures of the prepared samples were characterized by focused ion beam scanning electron microscopy (FIB-SEM; Auriga, Zeiss) and transmission electron microscopy (TEM; Talos F200S, FEI, and JEM-2200FS, JEOL, at Zhengzhou University and University of Science and Technology Beijing, respectively). The scanning transmission electron microscopy (STEM) images and the elemental mapping images were obtained by double spherical aberration corrected analytical field emission TEM (JEM-ARM300F) combined with high-angle annular dark-field (HAADF) techniques. The chemical compositions of the samples were investigated by using SEM with energy dispersive spectroscopy (EDS) and inductively coupled plasma mass spectrometry (ICP-MS; NWR-213). The crystallographic information was characterized by employing a powder X-ray diffractometer (XRD; Empyrean, Malvern Panalytical) with Cu K$\alpha$. The electronic structures and the phase compositions of the samples were obtained via X-ray absorption near edge structure (XANES) with the BL11B beamline at the Shanghai Synchrotron Radiation Facility, X-ray photoelectron spectroscopy (XPS; AXIS Supra), and laser Raman spectrometry (532 nm, Renishaw).

### 2.5 Electrochemical measurement

The electrochemical data were measured using a classical three-electrode system of CHI660E electrochemical workstation (Chenhua Instruments, Shanghai, China) at RT. A glassy carbon electrode (3 mm in diameter), a saturated calomel electrode (SCE), and a Pt wire were used as working, reference, and counter electrodes, respectively. To obtain the homogeneous catalyst ink by sonification, 4 mg of catalyst powder was dissolved in 4 mL of ethanol. According to the composition

ratio of Pt, the corresponding volume of catalyst inks were taken to cover the working electrode surface evenly with the same loading density of about 10 $\mu g_{Pt} \cdot cm^{-2}$. After the electrode surface was thoroughly dried, 5 μL of the Nafion membrane solution (5 wt.%) was dropped onto the working electrode and was dried overnight. Prior to the electrocatalytic test, all electrolytes were ventilated with $N_2$ for 30 min to remove the O interference.

### 2.6 First-principles calculation

The first-principles calculations were conducted using the Vienna *ab initio* simulation package (VASP) [25] with projector-augmented wave (PAW) potentials [26, 27] and Perdew-Burke-Ernzerh of generalized gradient approximation (PBE-GGA) [28] for the exchange–correlation functionals. To simulate CO adsorption onto the small clusters deposited on the substrate, a periodic slab model was adopted for the monolayer graphene substrate with a 5 × 3 rectangle supercell. For the nanostructure model, we used an 8 × 8 graphene (CoNC) rhombic supercell to match the 7 × 7 metal bi-layer films for reducing the lattice mismatch within 3%. The thickness of the vacuum layer was 15 Å. all atoms were fully relaxed along the calculated forces until all of the residual force components were less than 0.01 eV.

## 3 Results and discussion

The formation procedure of PtAu loading on Co and N co-doped carbon nanoframes derived from MOFs is briefly described in Scheme 1. This process consists mainly of two steps: preparation of the support material and loading of Pt and Au. In the first step, as a typical MOF material, ZIF-67 with well-defined rhombic dodecahedral morphology was fabricated by applying a hydrothermal method (Fig. S1 in the Electronic Supplementary Material (ESM)). After carbonization and acid treatment, CoNC NFs with cubic structures were obtained. As shown in Fig. S1(c) in the ESM, the size of CoNC NFs was about 177 nm (Fig. S2 in the ESM), although the surface exhibited slight collapse and shrinkage on owing mainly to the trend of Co NP aggregation during the carbonization process [29]. Afterward, the Pt and Au were reduced by different excess reducing agents and were then deposited on the CoNC NFs. The composition information of the PtAu/CoNC was determined by ICP-MS (Table S1 in the ESM). The Pt/Au atomic ratio was in good agreement with the initial feed ratio, indicating that the metal precursors were reduced completely with no resource waste.

The morphological and structural features of the as-prepared series of PtAu/CoNC samples were characterized by SEM, as shown in Fig. 1(a) and Fig. S3 in the ESM. The profiles of samples with different Pt/Au ratios were almost identical, with all in cubic form exhibiting collapsed surfaces similar to those of the substrate material CoNC NFs. To more effectively describe and discuss the structural characteristics of the obtained samples, PtAu/CoNC-3 was taken as a representative for the detailed analysis. According to the typical SEM image of PtAu/CoNC-3 in Fig. 1(a), large amounts of NPs were easily distinguished from the surface of the collapsed cube, which should belong to Pt or Au. The inset in Fig. 1(a) shows statistical

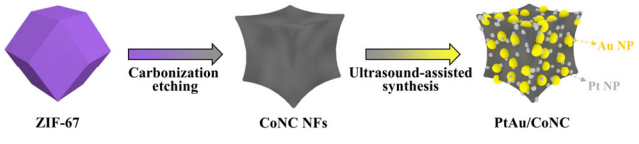


**Scheme 1** Schematic illustration of the PtAu/CoNC preparation process.

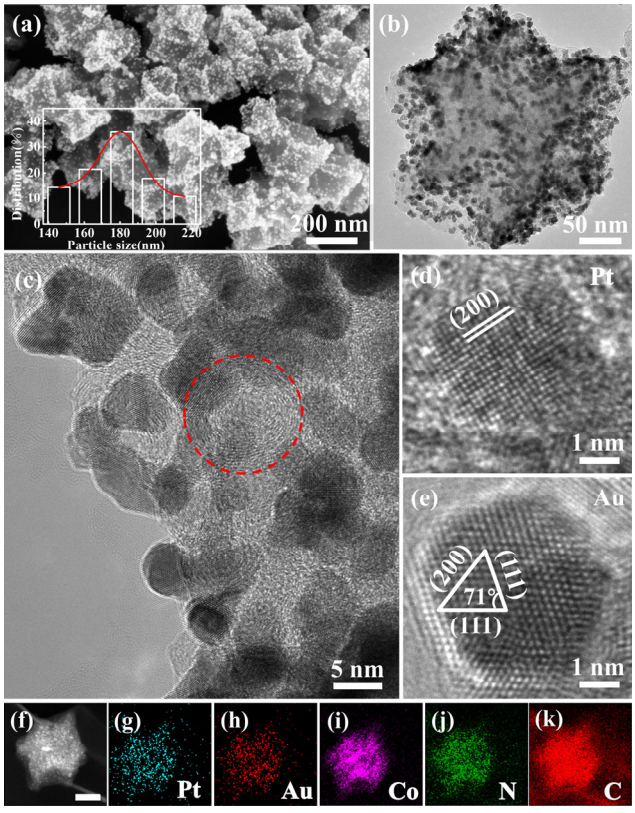


**Figure 1** Representative (a) SEM image, (b) TEM image and (c)–(e) HRTEM images of PtAu/CoNC-3. The inset in (a) shows the corresponding size distribution. (f)–(k) HAADF-STEM image of PtAu/CoNC-3 and the corresponding element mapping images. All scales are 100 nm.

histograms for the nanoparticle size, further confirming that the average size of the PtAu/CoNC, at ~ 178 nm, is almost as same as that of the CoNC NFs. As shown in Fig. S4 in the ESM, the corresponding EDS data of PtAu/CoNC-3 indicate that the metal contents were very close to the feed ratio. Figure 1(b) presents a TEM image of a single PtAu/CoNC-3, which shows that the Pt and Au NPs were uniformly and densely distributed on the support of the CoNC NFs, which is consistent with the SEM results.

The high-resolution TEM (HRTEM) images shown in Figs. 1(c)–1(e) reveal more definite and detailed information of the PtAu/CoNC-3. Figure 1(c) shows partial overlap in the distribution of metal particles and significant graphitization of the substrate material (red circles), all of which are beneficial for accelerating the electron transfer in the catalytic process and improving the efficiency of the FAO reaction [30].The different lattice spacings can be measured according to the HRTEM images in Figs. 1(d) and 1(e), corresponding to the (200) plane of Pt (0.198 nm) and the (111) and (200) planes of Au (0.234 and 0.202 nm), respectively [31, 32]. A small deviation from the standard value was evident, indicating the presence of some degree of lattice distortion [20, 33]. The elemental distribution profile was obtained through STEM-EDS mapping, with the typical results of an individual PtAu/CoNC-3 shown in Figs. 1(f)–1(k). These results reveal that all component elements were evenly distributed throughout the nanoparticle with no composition segregation.

The general crystallographic information of the Pt/CoNC and PtAu/CoNC samples were confirmed by the XRD patterns, as shown in Figs. 2(a) and 2(b), with the Pt/Au ratio of PtAu/CoNC-1, -2, -3 given as 4:1, 2:1, and 1:1, respectively. All obtained products exhibited broad Bragg peaks, indicating their small particle size, which is consistent with the above

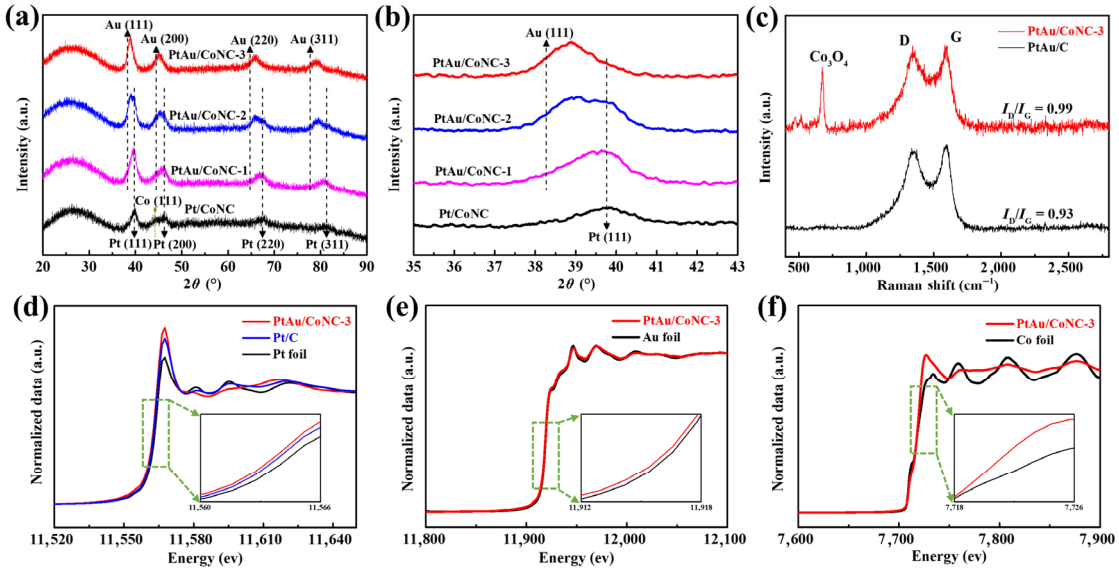


**Figure 2** (a) Full and (b) partial enlargement of XRD spectra for Pt/CoNC and PtAu/CoNC. The dashed lines show the standard diffraction data of the Pt and Au crystals. (c) Representative Raman spectra of PtAu/CoNC-3 and PtAu/C. (d) Pt $L_3$-edge XANES spectra of Pt foil, PtAu/CoNC-3, and Pt/C. (e) Au $L_3$-edge XANES spectra of Au foil and PtAu/CoNC-3. (f) Co K-edge XANES spectra of Co foil and PtAu/CoNC-3.

morphological results. In Fig. 2(a), the representative diffraction peaks of Pt/CoNC are shown at 39.7°, 46.2°, 67.4°, and 81.2°, corresponding to the (111), (200), (220), and (311) planes of the Pt face-centered cubic (fcc), respectively. With an increase in Au content, as shown in Fig. 2(b), all diffraction peaks gradually moved to a smaller angle, and the lattice spacings became larger because the lattice constant of Au is slightly larger than that of Pt. In addition, Co peaks were obvious in the XRD patterns of the CoNC NFs (Fig. S5 in the ESM), whereas the diffraction peaks of Co could not be distinguished in the XRD patterns of the Pt/CoNC and PtAu/CoNC samples. This could be attributed to its low crystallinity after acid etching.

We then examined the substrate and explored the existence of carbon in the nanoframe using Raman spectroscopy. Figure 2(c) shows two dominant Raman peaks at 1,360 and 1,590 $cm^{-1}$ assigned to the D and G bands of graphene, respectively. In general, the intensity of the D band represents the degree of disorder and the number of defects in the material, whereas that of the G band represents the graphitization degree of the carbon material [34, 35]. According to the calculation, the intensity ratios ($I_D/I_G$) of PtAu/CoNC-3 and PtAu/C are about 0.99 and 0.93, respectively, suggesting that elemental co-doping had little effect on the graphitization of carbon [36, 37]. In addition, compared with PtAu/C, the Raman spectrum of PtAu/ CoNC showed an extra peak at 677 $cm^{-1}$ corresponding to the characteristic peak of $Co_3O_4$. This indicates that part of the Co existed in the form of oxide [38].

To investigate the local electronic structure and coordination environment of Pt, Au, and Co in the PtAu/CoNC-3, XANES was employed for characterization [39, 40]. The normalized white line intensity of the Pt $L_3$-edge in the PtAu/CoNC-3 is close to that of the Pt/C and higher than that of the Pt foil, which indicates that $Pt^{x+}$ could exist in PtAu/CoNC-3 and Pt/C (Fig. 2(d)) [41]. In contrast, the normalized white line intensity of the Au $L_3$-edge in the PtAu/CoNC-3 essentially overlapped the Au foil, suggesting the dominance of $Au^0$ in the PtAu/CoNC-3, as shown in Fig. 2(e). Figure 2(f) shows that the white line of Co in the PtAu/CoNC-3 is clearly higher than that of the Co foil, indicating that the Co atoms in PtAu/ CoNC-3 carry positive charges. As shown in the inset in Figs. 2(d)–2(f), the energies of Pt, Au, and particularly Co all shifted from their corresponding metal foils, verifying the existence of electron interaction [40]. This phenomenon will be discussed in detail in the XPS analysis.

The full survey scan XPS spectrum in Fig. 3(a) confirms that the Pt, Au, Co, N, C, and O elements coexist in the near-surface of the prepared samples. The high-resolution spectra of Pt 4f and Au 4f are shown in Figs. 3(b) and 3(c), respectively, both of which contain two pairs of peaks from the spin–orbital splitting of $4f_{7/2}$ and $4f_{5/2}$. The two characteristic peaks of metallic Pt ($Pt^0$) were located at 71.3 and 74.7 eV, whereas those of ionic Pt ($Pt^{2+}$) occurred at 72.9 and 76.3 eV [42]. A comparison between the integrated areas revealed that the main surface species of Pt in the catalyst is metallic Pt ($Pt^0$). As shown in Fig. 3(c), the surface species of Au was only metallic Au ($Au^0$) with characteristic peaks located at 83.9 and 87.6 eV, which is strongly consistent with the XANES results. Compared with the standard Pt 4f peaks at 70.9 and 74.3 eV, the surface binding energy ($E_b$) of the metallic Pt in the PtAu/CoCN-3 positively shifted by 0.4 eV (Fig. 3(b)). This indicates a down shift in the d-band center of the Pt [43]. On the contrary, the $E_b$ of the Au 4f peaks shift negatively compared with the standard Au 4f peaks (84.0 and 87.7eV) (Fig. 3(c)). Both shifts of the $E_b$ indicate changes in the corresponding electronic structures, which could be attributed to interaction among the Pt, Au, and CoNC NFs [44, 45].

The high-resolution spectrum of Co 2p in Fig. 3(d) shows two characteristic peaks at binding energies of 781.3 and 796.3 eV assigned for Co $2p_{3/2}$ and Co $2p_{1/2}$, respectively, which can be deconvoluted to $Co^0$ at 781.1 and 796.2 eV and $Co^{2+}$ at 785.2 and 800.9 eV. Of these, the presence of $Co^{x+}$ has been confirmed in the Raman data (677 $cm^{-1}$). Two main types of N, pyridinic-N (398.7 eV) and pyrrolic-N (400.3 eV), are indicated in the high-resolution spectrum of N 1s in Fig. 3(e). Interestingly, a comparison of the integrated areas revealed more pyridinic-N in the sample, which would favor the catalytic performance [46]. In the high-resolution spectra of C 1s shown in Fig. 3(f), several characteristic peaks at 284.6, 285.7, and 288.5 eV correspond to C in $sp^2$-hybridized graphitic carbon, C–O–C and C–N, and O–C=O, respectively [24].

Before investigating the effect of different Au compositions in the PtAu/CoNC catalysts on catalytic pathway and catalytic efficiency of FAO, we identified the electrochemically active

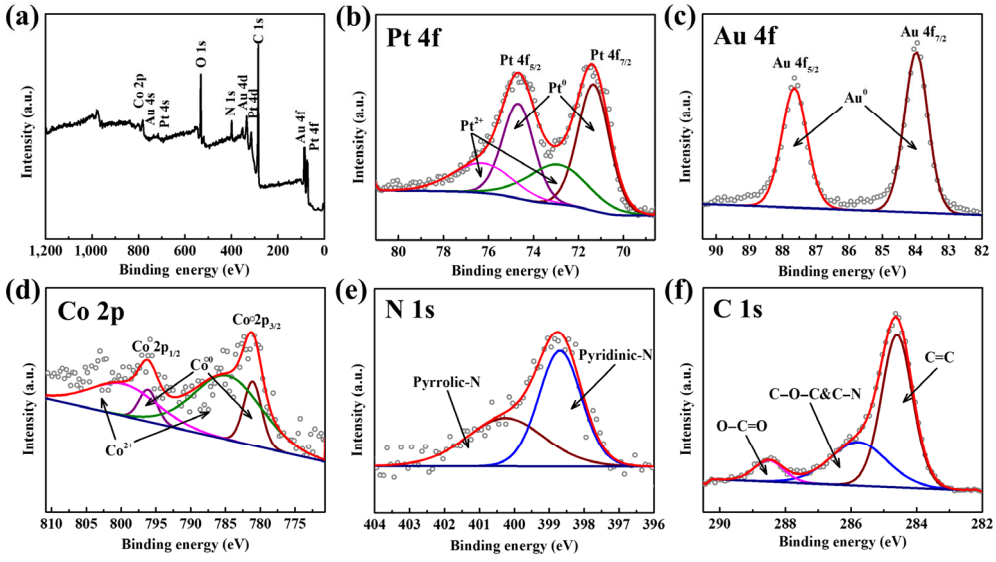


**Figure 3** High-resolution XPS spectra of (a) the survey scan spectrum, (b) Pt 4f, (c) Au 4f, (d) Co 2p, (e) N 1s, and (f) C 1s peaks in PtAu/CoNC-3.

surface areas (ECSAs) of each catalyst. The cyclic voltammetry (CV) curves of the catalysts were obtained in an aqueous solution of 0.5 M $H_2SO_4$ saturated with $N_2$, as summarized in Fig. S6 in the ESM. The ECSAs were determined on the basis of the hydrogen desorption region after subtraction of the double-layer charge [47]. The PtAu/CoNC-3 exhibited a higher ECSA value among the as-prepared catalysts loaded on CoNC NFs, indicating better Pt utilization in the PtAu/CoNC-3 catalyst [11].

To gain further insight into the effect of the Au content on the FAO pathway, the linear sweep voltammetry (LSV) was measured from −0.1 V to +1.0 V in the mixed solution of 0.5 M $H_2SO_4$ and 1 M HCOOH at a scan rate of 50 mV·s$^{-1}$. As mentioned above, the FAO reaction usually follows two oxidation pathways:

$$HCOOH \rightarrow CO_2 + 2H^+ + 2e^- \quad (1)$$

and

$$HCOOH \rightarrow CO_{ads} + H_2O \rightarrow CO_2 + 2H^+ + 2e^- \quad (2)$$

where Eqs. (1) and (2) represent direct and indirect oxidation pathways, respectively. These two oxidation pathways correspond to two pronounced peaks in the LSV curves shown in Fig. 4(a): the lower potential peak (pI) and the higher potential peak (pII). The direct oxidation pathway proceeds through the dehydrogenation reaction, where the C–H and O–H bonds are broken, and the formic acid is directly oxidized to $CO_2$. This process is capable of occurring more rapidly and efficiently at a low potential and corresponds to pI in the LSV curves. The indirect pathway originated from the dehydration reaction, where the C–O single bond and the C–H bond are broken, and formic acid forms the adsorbent $CO_{ads}$ which will be oxidized to $CO_2$. This corresponds to pII in the LSV curves. During the indirect pathway, the $CO_{ads}$ caused by dehydration will strongly adsorb onto and poison the catalyst surface, reducing the number of active sites available for the direct oxidation pathway, and the direct pathway is inhibited [6, 48, 49]. Figure 4(a) shows that the indirect oxidation pathway is dominant when the content of Au is 0 (Pt/CoNC) or lower (PtAu/CoNC-1). As the Au content increases in PtAu/ CoNC, the Au atoms shield the Pt form CO poisoning. Then, the direct pathway is gradually enhanced, and the indirect pathway is therefore weakened. When the Pt/Au atomic ratio was 1:1 (PtAu/CoNC-3), the FAO reaction pathway was almost entirely dominated by the direct oxidation pathway shown in Fig. 4(a). This is attributed to the presence of Pt and Au in ideal proportions and optimal cooperation with the co-doped substrate. In this case, the PtAu/CoNC-3 showed the highest peak current density of pI ($J_{pI}$) among the as-prepared samples loaded on the CoNC NFs; accordingly, the Pt utilization was optimal. The $J_{pI}$ rapidly decreased with further increases in Au, which could be attributed to the excessive Au blocking the active sites of Pt, resulting in degradation of catalyst activity (Fig. S7 in the ESM) [50]. The histogram in Fig. 4(b) corresponding to Fig. 4(a) illustrates the intrinsic catalytic activity of the catalysts after ECSA- and mass-normalization of $J_{pI}$. As shown in Fig. 4(b), PtAu/CoNC with different Pt/Au compositions all showed better FAO activity than Pt/CoNC, indicating that the addition of Au also improved the utilization of Pt when the substrate material was CoNC NFs. Among them, the Pt/Au CoNC-3 with a Pt/Au ratio of 1:1 exhibited the best specific activity and mass activity, which were 25.5 and 25.3 times higher than those of the Pt/CoNC, respectively. Through the above discussion, we explored the optimal atomic ratio of Pt and Au co-loading onto CoNC NFs. Interestingly, we also found that the oxidation pathways of FAO can be effectively selected by modulating the Au content, which is significant for improving the catalytic

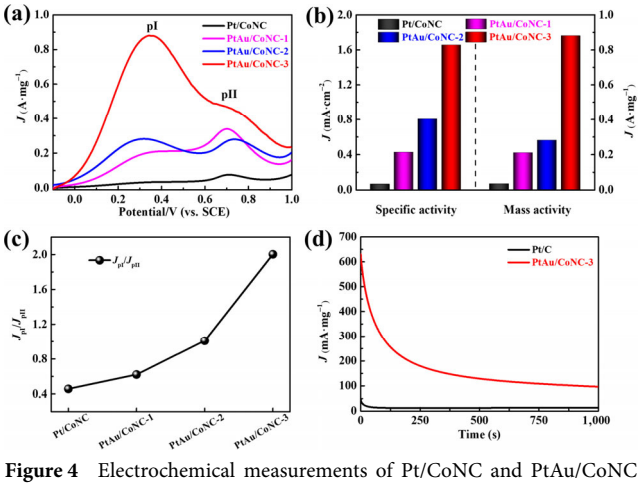


**Figure 4** Electrochemical measurements of Pt/CoNC and PtAu/CoNC catalysts in aqueous solutions of 1 M HCOOH and 0.5 M $H_2SO_4$. (a) Linear sweep voltammetry (LSV) curves normalized by Pt weight. (b) Corresponding specific activities and mass activities. (c) CO tolerance ($J_{pI}/J_{pII}$). (d) Chronoamperometry curves measured at 0.23 V.

ability of the Pt-based catalyst.

The peak current density ratio of the two oxidation pathways ($J_{pI}/J_{pII}$) can directly reveal the dominant reaction pathway in FAO and the tolerance to CO poisoning [51, 52]. As shown in Fig. 4(c), the values of $J_{pI}/J_{pII}$ became larger as the Au content increased, indicating that the direct oxidation pathway became more dominant and the resistance to CO poisoning was higher. This result can more intuitively illustrate that the Au content can modulate the catalytic oxidation pathways of FAO and thus the catalytic performance of the catalyst. Moreover, an appropriate atomic ratio can enhance the collaborative ability between the atoms of different elements, which is beneficial for improving the dehydrogenation selectivity of the direct oxidation pathway of FAO and thus for obtaining high catalytic activity.

In terms of practical application, the stability of the catalyst is also a crucial indicator and can be tested in an aqueous solution of 0.5 M $H_2SO_4$ mixed with 1 M HCOOH. As shown in Fig. 4(d), after 1,000 s, the PtAu/CoNC-3 still had a greater current density compared with that of the Pt/C. This is because the direct oxidation pathway is dominant in PtAu/CoNC-3-catalyzed FAO and does not produce many intermediates during the reaction, which greatly reduces the chance of catalyst poisoning. In contrast, the main oxidation pathway of the Pt/C is indirect oxidation, with a large number of intermediates adsorbed onto the active sites, leading to the deactivation of numerous active sites. The difference in stability between the two catalysts also indicates that modulation of the oxidation pathways has a significant effect on the practical application of the catalysts.

To thoroughly explore whether the CoNC NFs substrate has an influence on the oxidation pathway selection and the catalytic efficiency of FAO, the PtAu (Pt:Au = 1:1) and PtAuCo (Pt:Au:Co = 1:1:1) were loaded on carbon black (Figs. 5(a) and 5(b)). It is worth mentioning that different from that of PtAu/CoNC, the particle sizes of the metallic NPs gradually increased with an increase in the Au content in the PtAu/C (Fig. S8 in the ESM). This indicates that CoNC NFs might be beneficial for inhibiting the agglomeration and growth of NPs. Typical LSV curves of FAO catalyzed with Pt/C, PtAu/C, PtAuCo/C, and PtAu/CoNC-3 are shown in Fig. 5(d). It is clear that loading the same proportion of Pt/Au on the CoNC NFs and carbon black also had a significant effect on the oxidation pathway and that the value of $J_{pI}/J_{pII}$ provided a more intuitive view of this effect. Figure 5(e) shows that the $J_{pI}/J_{pII}$ values of PtAu/C, PtAuCo/C, and PtAu/CoNC-3 were higher than that of the Pt/C, which again confirms that the addition of Au can promote the direct oxidation pathway of FAO. Furthermore, the $J_{pI}/J_{pII}$ values of PtAu/C (0.78) and PtAuCo/C (0.92) were comparable, indicating that the Co had little influence on the preference of the FAO oxidation pathway. In contrast, the $J_{pI}/J_{pII}$ value of the PtAu/CoNC was higher than that of the other three catalysts, particularly that of PtAuCo/C. This suggests that CoNC NFs but not Co facilitate the preferential selection of the FAO direct oxidation pathway.

The mass and specific activities shown Fig. 5(f) were obtained by normalizing the $J_{pI}$ by the mass and the ECSA value, respectively. The mass activity and specific activity of four catalysts showed similar tendencies, with PtAu/CoNC having the largest value, followed by PtAuCo/C, PtAu/C, and finally Pt/C. This indicates that CoNC NFs play a vital role in promoting the achievement of larger $J_{pI}$. The enhancement of direct oxidation currents by CoNC NFs is attributed mainly to the co-doping of Co and N, which can have stronger interactions with Pt and Au and can also produce more lattice distortions and Co–$N_x$ active sites [24].

To further investigate the CO tolerance of catalysts, a CO stripping test was conducted in an aqueous solution of 0.5 M $H_2SO_4$ saturated with a CO environment. The corresponding voltammograms of PtAu/C, Pt/CoNC, and PtAu/CoNC-3 are presented in Fig. 6(a), where the currents in the voltammograms were normalized to the electrode geometric area. The peak potentials of the PtAu/CoNC-3, Pt/CoNC, and PtAu/C catalysts were 0.628, 0.640, and 0.652 V. Moreover, the PtAu/CoNC-3 had the lowest onset potential of a CO stripping peak, which means that only a lower potential needed to be supplied to the PtAu/CoNC-3 for oxidation of easily toxic intermediates such as CO during the catalytic reaction. This is attributed mainly to the synergistic and electronic effects of the metallic elements and their interaction with the support material, which can effectively modulate the electronic structure of Pt and weaken the adsorption of Pt to CO, thus enhancing the CO tolerance of the catalyst [22, 53, 54].

To further explore the synergistic effect of Pt and Au atoms on CO adsorption in the electrocatalytic process, we performed first-principles calculations on the CO adsorptions on two prototypical systems: small $Pt_nAu_m$ clusters and PtAu nanostructures deposited on the CoNC and graphene substrates. Here, for simplicity, $Pt_4$/CoNC, $Pt_2Au_2$/CoNC, and $Pt_2Au_2$/C were considered in our cluster model, and bi-layered Pt and

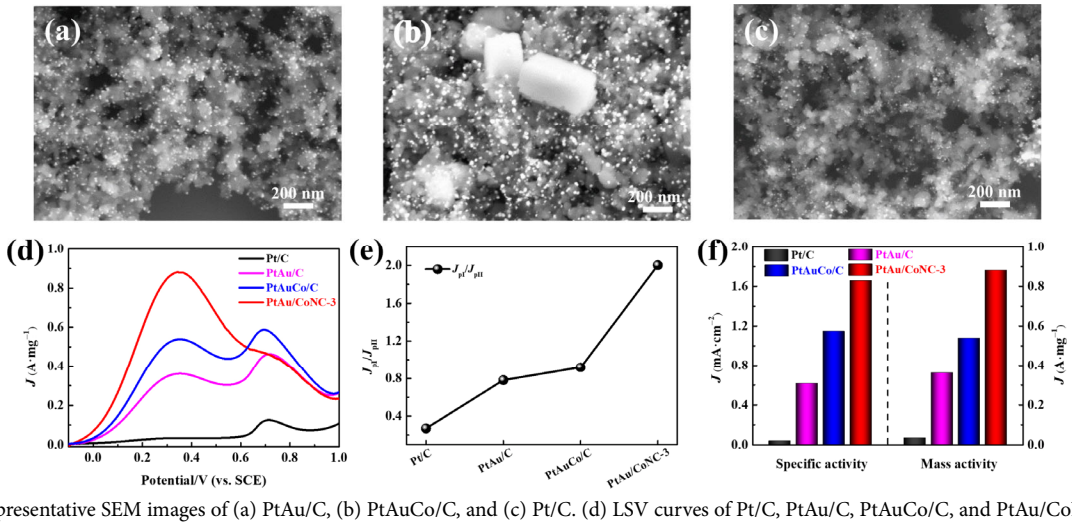


**Figure 5** Representative SEM images of (a) PtAu/C, (b) PtAuCo/C, and (c) Pt/C. (d) LSV curves of Pt/C, PtAu/C, PtAuCo/C, and PtAu/CoNC-3 catalysts normalized by the Pt weight in aqueous solutions of 1 M HCOOH and 0.5 M $H_2SO_4$. (e) CO tolerance ($J_{pI}/J_{pII}$). (f) Corresponding specific activities and mass activities.

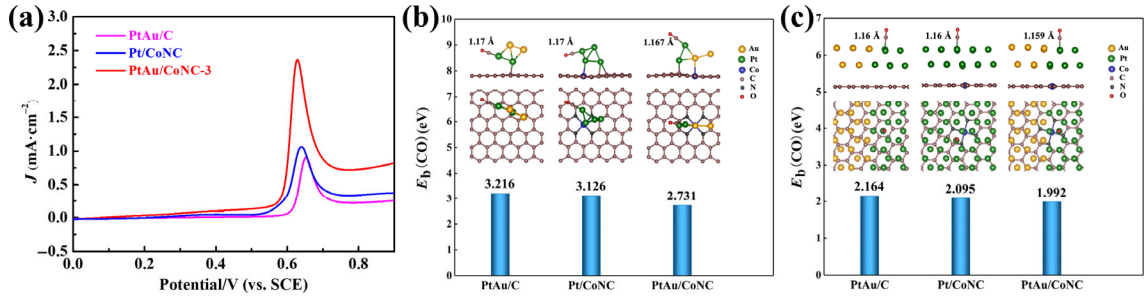


**Figure 6** (a) CO stripping voltammograms of different electrodes in 0.5 M $H_2SO_4$ with a sweep rate of 50 mV·s$^{-1}$. (b) and (c) First-principles calculation of binding energy ($E_b$) for CO binding on PtAu/C, Pt/CoNC, and PtAu/CoNC-3. (b) and (c) show $Pt_nAu_m$ clusters and PtAu nanostructures models, respectively.

PtAu films were selected to mimic the PtAu nanostructures, as shown in Figs. 6(b) and 6(c), respectively. For both models, the role of Au and CoNC in reducing the binding strength of the CO was confirmed. Specifically, as shown in Fig. 6(b), the $E_b$ of CO on the optimized $Pt_4$/CoNC complex was 3.126 eV; on $Pt_2Au_2$/CoNC, however, the $E_b$ was significantly reduced to 2.731 eV. Moreover, the calculated $E_b$ of the CO on $Pt_2Au_2$/C, at 3.216 eV, was larger than that on both $Pt_4$/CoNC and $Pt_2Au_2$/CoNC. It is important to note that the same trend was verified in the nanostructure model shown in Fig. 6(c). Therein, the calculated $E_b$ was 2.095, 1.992, and 2.164 eV when CO was adsorbed onto the Pt/CoNC, PtAu/CoNC, and PtAu/C complexes, respectively.

The results of the first-principles calculation and the CO stripping experiments are in good agreement, indicating that the adsorption capacity of the three catalysts for CO follows the order PtAu/CoNC < Pt/CoNC < PtAu/C. A comparison between Pt/CoNC and PtAu/CoNC revealed that the addition of Au can weaken the CO adsorption onto Pt, which is consistent with our expectation. Moreover, the difference between the CO absorption of PtAu/C and PtAu/CoNC indicates that CoNC NFs is more beneficial for weakening the CO adsorption than C, thus alleviating catalyst poisoning. Therefore, we conclude that Pt, Au, and CoNC NFs have good synergistic effects for exposing more active sites for the direct oxidation pathway by weakening the adsorption of CO onto the active site, which improves the catalytic performance of the Pt.

## 4 Conclusions

In this work, we discussed in depth the influence of different Au contents in PtAu/CoNC on the FAO oxidation pathway and obtained PtAu/CoNC catalyst with excellent catalytic performance. An increase in the Au content caused the direct oxidation pathway in FAO to gradually dominate. When the Pt/Au atomic ratio was 1:1, the FAO catalytic activity of the PtAu/CoNC sample greatly enhanced up to 26.0 times that of the Pt/C. Moreover, the PtAu/CoNC showed excellent performance in CO stripping experiments, with a lower onset potential of 0.024 V compared with that of PtAu/C confirmed using first-principles calculation. This excellent performance is attributed to the synergistic effects of Pt and Au, Co–$N_x$ active site formation by co-doping, graphitized carbon substrate, and electron transfer between the metals and support material.

## Acknowledgements

Thanks for the financial support from the National Natural Science Foundation of China (Nos. 51801188, 12034002, and 51971025), the China Postdoctoral Science Foundation (No. 2018M632792), program for the Innovation Team of Science and Technology in University of Henan (No. 20IRTSTHN014), Excellent Youth Foundation of He'nan Scientific Committee (No. 202300410356), the CAS Interdisciplinary Innovation Team (No. JCTD-2019-01), and Beijing Natural Science Foundation (No. 2204085). The Center of Advanced Analysis & Gene Sequencing of Zhengzhou University is acknowledged for providing characterization facilities. Shanghai Synchrotron Radiation Facility (SSRF) is acknowledged for providing X-ray absorption near edge structure (XANES) test at the BL11B beamline.

**Electronic Supplementary Material**: Supplementary material (SEM images, EDS spectra, XRD patterns, CV curves, anodic polarization curve and composition table) is available in the online version of this article at http://doi.org/10.1007/s12274-021-3629-z.

## References

[1] Li, W.; Wang, D. D.; Zhang, Y. Q.; Tao, L.; Wang, T. H.; Zou, Y. Q.; Wang, Y. Y.; Chen, R.; Wang, S. Y. Defect engineering for fuel-cell electrocatalysts. *Adv. Mater.* **2020**, *32*, 1907879.

[2] Rejal, S. Z.; Masdar, M. S.; Kamarudin, S. K. A parametric study of the direct formic acid fuel cell (DFAFC) performance and fuel crossover. *Int. J. Hydrogen Energy* **2014**, *39*, 10267–10274.

[3] Jiang, X.; Xiong, Y. X.; Wang, Y. F.; Wang, J. X.; Li, N. X.; Zhou, J. C.; Fu, G. T.; Sun, D. M.; Tang, Y. W. Treelike two-level $Pd_xAg_y$ nanocrystals tailored for bifunctional fuel cell electrocatalysis. *J. Mater. Chem. A* **2019**, *7*, 5248–5257.

[4] Li, F. H.; Guo, Y. Q.; Liu, Y.; Qiu, H. X.; Sun, X. Y.; Wang, W.; Liu, Y.; Gao, J. P. Fabrication of Pt–Cu/RGO hybrids and their electrochemical performance for the oxidation of methanol and formic acid in acid media. *Carbon* **2013**, *64*, 11–19.

[5] Goswami, C.; Saikia, H.; Tada, K.; Tanaka, S.; Sudarsanam, P.; Bhargava, S. K.; Bharali, P. Bimetallic palladium–nickel nanoparticles anchored on carbon as high-performance electrocatalysts for oxygen reduction and formic acid oxidation reactions. *ACS Appl. Energy Mater.* **2020**, *3*, 9285–9295.

[6] Jiang, X.; Liu, Y.; Wang, J. X.; Wang, Y. F.; Xiong, Y. X.; Liu, Q.; Li, N. X.; Zhou, J. C.; Fu, G. T.; Sun, D. M. et al. 1-Naphthol induced $Pt_3Ag$ nanocorals as bifunctional cathode and anode catalysts of direct formic acid fuel cells. *Nano Res.* **2019**, *12*, 323–329.

[7] Betts, A.; Briega-Martos, V.; Cuesta, A.; Herrero, E. Adsorbed formate is the last common intermediate in the dual-path mechanism of the electrooxidation of formic acid. *ACS Catal.* **2020**, *10*, 8120–8130.

[8] Calderón-Cárdenas, A.; Hartl, F. W.; Gallas, J. A. C.; Varela, H. Modeling the triple-path electro-oxidation of formic acid on platinum: Cyclic voltammetry and oscillations. *Catal. Today* **2021**, *359*, 90–98.

[9] Wang, Y.; Jiang, X.; Fu, G. T.; Li, Y. H.; Tang, Y. D.; Lee, J. M.; Tang, Y. W. $Cu_5Pt$ dodecahedra with low-Pt content: Facile synthesis and outstanding formic acid electrooxidation. *ACS Appl. Mater. Interfaces* **2019**, *11*, 34869–34877.

[10] Krstajić Pajić, M. N.; Stevanović, S. I.; Radmilović, V. V.; Gavrilović-Wohlmuther, A.; Zabinski, P.; Elezović, N. R.; Radmilović, V. R.;

Gojković, S. L.; Jovanović, V. M. Dispersion effect in formic acid oxidation on PtAu/C nanocatalyst prepared by water-in-oil microemulsion method. *Appl. Catal. B Environ.* **2019**, *243*, 585–593.

[11] Guo, L. M.; Zhang, D. F.; Guo, L. Structure design reveals the role of Au for ORR catalytic performance optimization in PtCo-based catalysts. *Adv. Funct. Mater.* **2020**, *30*, 2001575.

[12] Zhang, Q. Q.; Liu, J. L.; Xia, T. Y.; Qi, J.; Lyu, H. C.; Luo, B. Y.; Wang, R. M.; Guo, Y. Z.; Wang, L. H.; Wang, S. G. Antiferromagnetic element Mn modified PtCo truncated octahedral nanoparticles with enhanced activity and durability for direct methanol fuel cells. *Nano Res.* **2019**, *12*, 2520–2527.

[13] Lv, F.; Zhang, W. Y.; Sun, M. Z.; Lin, F. X.; Wu, T.; Zhou, P.; Yang, W. X.; Gao, P.; Huang, B. L.; Guo, S. J. Au clusters on Pd nanosheets selectively switch the pathway of ethanol electrooxidation: Amorphous/crystalline interface matters. *Adv. Energy Mater.* **2021**, *11*, 2100187.

[14] Mistry, H.; Varela, A. S.; Kühl, S.; Strasser, P.; Cuenya, B. R. Nanostructured electrocatalysts with tunable activity and selectivity. *Nat. Rev. Mater.* **2016**, *1*, 16009.

[15] Zhang, S.; Shao, Y. Y.; Liao, H. G.; Liu, J.; Aksay, I. A.; Yin, G. P.; Lin, Y. H. Graphene decorated with PtAu alloy nanoparticles: Facile synthesis and promising application for formic acid oxidation. *Chem. Mater.* **2011**, *23*, 1079–1081.

[16] Cappellari, P. S.; García, G.; Florez-Montaño, J.; Barbero, C. A.; Pastor, E.; Planes, G. A. Enhanced formic acid oxidation on polycrystalline platinum modified by spontaneous deposition of gold. Fourier transform infrared spectroscopy studies. *J. Power Sources* **2015**, *296*, 290–297.

[17] Kim, S. H.; Jeong, H.; Kim, J.; Lee, I. S. Fabrication of supported AuPt alloy nanocrystals with enhanced electrocatalytic activity for formic acid oxidation through conversion chemistry of layer-deposited $Pt^{2+}$ on au nanocrystals. *Small* **2015**, *11*, 4884–4893.

[18] Zheng, F. L.; Wong, W. T.; Yung, K. F. Facile design of Au@Pt core-shell nanostructures: Formation of Pt submonolayers with tunable coverage and their applications in electrocatalysis. *Nano Res.* **2014**, *7*, 410–417.

[19] Li, D. W.; Meng, F. H.; Wang, H.; Jiang, X. J.; Zhu, Y. Nanoporous aupt alloy with low Pt content: A remarkable electrocatalyst with enhanced activity towards formic acid electro-oxidation. *Electrochim. Acta* **2016**, *190*, 852–861.

[20] Fan, H. S.; Cheng, M.; Wang, L.; Song, Y. J.; Cui, Y. M.; Wang, R. M. Extraordinary electrocatalytic performance for formic acid oxidation by the synergistic effect of Pt and Au on carbon black. *Nano Energy* **2018**, *48*, 1–9.

[21] Chen, X. M.; Wu, G. H.; Chen, J. M.; Chen, X.; Xie, Z. X.; Wang, X. R. Synthesis of "clean" and well-dispersive Pd nanoparticles with excellent electrocatalytic property on graphene oxide. *J. Am. Chem. Soc.* **2011**, *133*, 3693–3695.

[22] Lv, Y. H.; Li, X. W. PtCo/N-doped carbon sheets derived from a simple pyrolysis of graphene oxide/ZIF-67/$H_2PtCl_6$ composites as an efficient catalyst for methanol electro-oxidation. *Int. J. Hydrogen Energy* **2020**, *45*, 12766–12776.

[23] Ahn, S. H.; Klein, M. J.; Manthiram, A. 1D Co- and N-doped hierarchically porous carbon nanotubes derived from bimetallic metal organic framework for efficient oxygen and tri-iodide reduction reactions. *Adv. Energy Mater.* **2017**, *7*, 1601979.

[24] Ren, W. N.; Zang, W. J.; Zhang, H. F.; Bian, J. L.; Chen, Z. F.; Guan, C.; Cheng, C. W. PtCo bimetallic nanoparticles encapsulated in N-doped carbon nanorod arrays for efficient electrocatalysis. *Carbon* **2019**, *142*, 206–216.

[25] Kresse, G.; Furthmuller, J. Efficient iterative schemes for *ab initio* total-energy calculations using a plane-wave basis set. *Phys. Rev B* **1996**, *54*, 11169–11186.

[26] Blöchl, P. E. Projector augmented-wave method. *Phys. Rev. B* **1994**, *50*, 17953–17979.

[27] Kresse, G.; Joubert, D. From ultrasoft pseudopotentials to the projector augmented-wave method. *Phys. Rev. B* **1999**, *59*, 1758–1775.

[28] Perdew, J. P.; Burke, K.; Ernzerhof, M. Generalized gradient approximation made simple. *Phys. Rev. Lett.* **1996**, *77*, 3865–3868.

[29] Zhu, J. Y.; Qu, T.; Su, F. M.; Wu, Y. Q.; Kang, Y.; Chen, K. F.; Yao, Y. C.; Ma, W. H.; Yang, B.; Dai, Y. N. et al. Highly dispersed Co nanoparticles decorated on a N-doped defective carbon nanoframework for a hybrid Na–air battery. *Dalton Trans.* **2020**, *49*, 1811–1821.

[30] Wu, X.; Meng, G.; Liu, W. X.; Li, T.; Yang, Q.; Sun, X. M.; Liu, J. F. Metal-organic framework-derived, Zn-doped porous carbon polyhedra with enhanced activity as bifunctional catalysts for rechargeable zinc-air batteries. *Nano Res.* **2018**, *11*, 163–173.

[31] Gao, D. W.; Li, S.; Song, G. L.; Zha, P. F.; Li, C. C.; Wei, Q.; Lv, Y. P.; Chen, G. Z. One-pot synthesis of Pt−Cu bimetallic nanocrystals with different structures and their enhanced electrocatalytic properties. *Nano Res.* **2018**, *11*, 2612–2624.

[32] Peng, Y.; Li, L. D.; Tao, R.; Tan, L. Y.; Qiu, M. N.; Guo, L. One-pot synthesis of Au@Pt star-like nanocrystals and their enhanced electrocatalytic performance for formic acid and ethanol oxidation. *Nano Res.* **2018**, *11*, 3222–3232.

[33] Li, F. M.; Ding, Y.; Xiao, X.; Yin, S. B.; Hu, M. C.; Li, S.; Chen, Y. From monometallic Au nanowires to trimetallic AuPtRh nanowires: Interface control for the formic acid electrooxidation. *J. Mater. Chem. A* **2018**, *6*, 17164–17170.

[34] Zhang, L. J.; Su, Z. X.; Jiang, F. L.; Yang, L. L.; Qian, J. J.; Zhou, Y. F.; Li, W. M.; Hong, M. C. Highly graphitized nitrogen-doped porous carbon nanopolyhedra derived from ZIF-8 nanocrystals as efficient electrocatalysts for oxygen reduction reactions. *Nanoscale* **2014**, *6*, 6590–6602.

[35] Sahu, S. C.; Samantara, A. K.; Dash, A.; Juluri, R. R.; Sahu, R. K.; Mishra, B. K.; Jena, B. K. Graphene-induced Pd nanodendrites: A high performance hybrid nanoelectrocatalyst. *Nano Res.* **2013**, *6*, 635–643.

[36] Zhang, D.; Ye, K.; Yao, Y. C.; Liang, F.; Qu, T.; Ma, W.; Yang, B.; Dai, Y. N.; Watanabe, T. Controllable synthesis of carbon nanomaterials by direct current arc discharge from the inner wall of the chamber. *Carbon* **2019**, *142*, 278–284.

[37] Li, G. N.; Zheng, K. T.; Li, W. S.; He, Y. C.; Xu, C. J. Ultralow Ru-induced bimetal electrocatalysts with a Ru-enriched and mixed-valence surface anchored on a hollow carbon matrix for oxygen reduction and water splitting. *ACS Appl. Mater. Interfaces* **2020**, *12*, 51437–51447.

[38] Zhao, Q.; Liu, Q. L.; Zheng, Y. F.; Han, R.; Song, C. F.; Ji, N.; Ma, D. G. Enhanced catalytic performance for volatile organic compound oxidation over *in-situ* growth of $MnO_x$ on $Co_3O_4$ nanowire. *Chemosphere* **2020**, *244*, 125532.

[39] Tian, X. L.; Zhao, X.; Su, Y. Q.; Wang, L. J.; Wang, H. M.; Dang, D.; Chi, B.; Liu, H. F.; Hensen, E. J. M.; Lou, X. W. et al. Engineering bunched Pt-Ni alloy nanocages for efficient oxygen reduction in practical fuel cells. *Science* **2019**, *366*, 850–856.

[40] Sun, Y. M.; Xue, Z. Q.; Liu, Q. L.; Jia, Y. L.; Li, Y. L.; Liu, K.; Lin, Y. Y.; Liu, M.; Li, G. Q.; Su, C. Y. Modulating electronic structure of metal-organic frameworks by introducing atomically dispersed Ru for efficient hydrogen evolution. *Nat. Commun.* **2021**, *12*, 1369.

[41] Qiao, B. T.; Wang, A. Q.; Yang, X. F.; Allard, L. F.; Jiang, Z.; Cui, Y. T.; Liu, J. Y.; Li, J.; Zhang, T. Single-atom catalysis of CO oxidation using $Pt_1/FeO_x$. *Nat. Chem.* **2011**, *3*, 634–641.

[42] Xu, K. X.; Xia, T. Y.; Zhou, L.; Li, S. F.; Cai, B.; Wang, R. M.; Guo, H. Z. Synthesization, characterization, and highly efficient electrocatalysis of chain-like Pt-Ni nanoparticles. *Acta Phys. Sin.* **2020**, *69*, 076101.

[43] Li, C. Z.; Yuan, Q.; Ni, B.; He, T.; Zhang, S. M.; Long, Y.; Gu, L.; Wang, X. Dendritic defect-rich palladium-copper-cobalt nanoalloys as robust multifunctional non-platinum electrocatalysts for fuel cells. *Nat. Commun.* **2018**, *9*, 3702.

[44] Lee, H. I.; Joo, S. H.; Kim, J. H.; You, D. J.; Kim, J. M.; Park, J. N.; Chang, H.; Pak, C. Ultrastable Pt nanoparticles supported on sulfur-containing ordered mesoporous carbon via strong metal-support interaction. *J. Mater. Chem.* **2009**, *19*, 5934–5939.

[45] Du, X. Q.; Liu, C.; Du, C.; Cai, P.; Cheng, G. Z.; Luo, W. Nitrogen-doped graphene hydrogel-supported NiPt-$CeO_x$ nanocomposites and their superior catalysis for hydrogen generation from hydrazine at room temperature. *Nano Res.* **2017**, *10*, 2856–2865.

[46] Zhao, S. L.; Yin, H. J.; Du, L.; He, L. C.; Zhao, K.; Chang, L.; Yin,

G. P.; Zhao, H. J.; Liu, S. Q.; Tang, Z. Y. Carbonized nanoscale metal–organic frameworks as high performance electrocatalyst for oxygen reduction reaction. *ACS Nano* **2014**, *8*, 12660–12668.

[47] Hu, Y. M.; Zhu, M. Z.; Luo, X.; Wu, G.; Chao, T. T.; Qu, Y. T.; Zhou, F. Y.; Sun, R. B.; Han, X.; Li, H. et al. Coplanar Pt/c nanomeshes with ultrastable oxygen reduction performance in fuel cells. *Angew. Chem., Int. Ed.* **2021**, *60*, 6533–6538.

[48] An, L.; Yan, H. J.; Li, B.; Ma, J.; Wei, H.; Xia, D. G. Highly active N–PtTe/reduced graphene oxide intermetallic catalyst for formic acid oxidation. *Nano Energy* **2015**, *15*, 24–32.

[49] Jiang, X.; Fu, G. T.; Wu, X.; Liu, Y.; Zhang, M. Y.; Sun, D. M.; Xu, L.; Tang, Y. W. Ultrathin AgPt alloy nanowires as a high-performance electrocatalyst for formic acid oxidation. *Nano Res.* **2018**, *11*, 499–510.

[50] Zhang, Q.; Yao, Z. Q.; Zhou, R.; Du, Y. H.; Yang, P. Fabrication of Ag/Au/Pt composite catalysts and their electrocatalytic oxidation for formic acid. *Acta Chim. Sin.* **2012**, *70*, 2149–2154.

[51] Yang, S.; Lee, H. Atomically dispersed platinum on gold nano-octahedra with high catalytic activity on formic acid oxidation. *ACS Catal.* **2013**, *3*, 437–443.

[52] Kim, Y.; Kim, H. J.; Kim, Y. S.; Choi, S. M.; Seo, M. H.; Kim, W. B. Shape- and composition-sensitive activity of Pt and PtAu catalysts for formic acid electrooxidation. *J Phys Chem C* **2012**, *116*, 18093–18100.

[53] Lim, K. H.; Chen, Z. X.; Neyman, K. M.; Rösch, N. Comparative theoretical study of formaldehyde decomposition on PdZn, Cu, and Pd surfaces. *J. Phys. Chem. B* **2006**, *110*, 14890–14897.

[54] Wang, R. M. The dynamics of the peel. *Nat. Catal.* **2020**, *3*, 333–334.